Water depth estimate and flood extent enhancement for satellite-based inundation maps

Andrea Betterle[1] and Peter Salamon[1]

[1]Europen Commission, Joint Reserach Centre, Ispra (Italy)

Correspondence: Andrea Betterle (andrea.betterle@ec.europa.eu)

Abstract.

Floods are extreme hydrological events that can reshape the landscape, transform entire ecosystems, and alter the relationship of humans and animals with the surrounding environment. Every year, fluvial and coastal floods claim thousands of human lives and cause billions of euros in direct damages and inestimable indirect losses, in both economical and in life-quality terms.

5   Monitoring the spatio-temporal evolution of floods is of fundamental importance in order to reduce their devastating consequences. Observing floods from space can make the difference: from this distant vantage point it is possible to monitor large areas consistently and, by leveraging multiple sensors on different satellites, it is possible to acquire a comprehensive overview on the evolution of floods at a global scale. Synthetic Aperture Radar (SAR) sensors in particular have proven extremely effective for flood monitoring, as they can operate day and night and in all weather conditions, with a highly discriminatory

10 power. On the other hand, SAR sensors are unable to reliably detect water in certain conditions, the most critical being urban areas. Furthermore, flood water depth – which is a fundamental variable for emergency response and impact calculations – cannot be estimated remotely. In order to address such limitations, this study proposes a framework for estimating flood water depths and enhancing satellite-based flood delineations, based on readily available topographical data. The methodology is specifically designed to accommodate, as additional inputs, masks delineating water bodies and/or areas that are excluded from

15 flood mapping. In particular, the method relies on simple morphological arguments to expand flooded areas to cover excluded regions, and to estimate water depths based on the terrain elevation of the boundaries between flooded and non-flooded areas. The underlying algorithm – named FLEXTH – is provided as Python code and is designed to run in an unsupervised mode in a reasonable time over areas of several hundred thousand square kilometers. This new tool aims to quantify and ultimately to reduce the impacts of floods, especially when used in synergy with the recently released Global Flood Monitoring product of

20 the Copernicus Emergency Management Service.

1 Introduction

Floods are among the most devastating of natural disasters, causing widespread destruction and loss of life across the globe (EMDAT, 2022; Douris and Kim, 2021). Accurate and timely flood mapping is essential for effective disaster management, facilitating early warnings, evacuation planning, proactive response and subsequent recovery (Voigt et al., 2016). In the past, flood mapping relied heavily on ground-based observations, which often proved insufficient for real-time monitoring due to limitations in spatial and temporal coverage. The advent of satellite remote sensing technology and advancements in data processing techniques have revolutionized flood mapping, offering substantial benefits in terms of accuracy, coverage, and timeliness of information delivery (Schumann and Moller, 2015; Salamon et al., 2021). With satellites, floods can be monitored remotely and continuously over vast and inaccessible areas. These aspects are especially relevant for vulnerable regions where risk mitigation strategies are lacking and the response to disasters might be inadequate.

The data obtained from satellites provides valuable insights into flood dynamics such as water extent and the progression of inundations over time (Spasova and Nedkov, 2019). This information is crucial for emergency response planning and post event recovery, ultimately contributing to saving human lives and mitigating social and economic impacts.

Among the satellite-borne sensors, optical sensors (i.e. those operating in the optical range of the electromagnetic spectrum) have long been used to map floods (e.g. Grimaldi et al. (2016)). However, despite the extensive coverage of optical satellite imagery, it is still challenging to map floods from space under certain circumstances, either in a supervised or an unsupervised mode. For example, optical sensors can not "see" at nighttime or through clouds. The latter limitations are especially problematic, since adverse meteorological conditions may be expected during extreme hydrological events.

More recently, Synthetic Aperture Radar sensors (SAR) have offered an effective alternative for flood mapping, thanks to their high capacity to discriminate surface waters (Clement et al., 2018; Jo et al., 2018; Pulvirenti et al., 2011). Operating in C-band microwave frequencies (i.e. between 4 and 8 Ghz), SAR sensors such as the one on board the Copernicus Sentinel-1 satellite, allow for an efficient and comprehensive assessment of floods worldwide, day and night and regardless of the weather conditions.

Despite these advantages, the efficacy of SAR sensors can be adversely affected in certain situations, including: i) low sensitivity, where dry/wet areas may be misclassified due to the presence of dense vegetation or urban areas; ii) water look-alike conditions, where the ground surface interacts with the incoming radar signal as if it were water (e.g. smooth or very dry surfaces, or wet snow).

Masking areas such as these, where SAR-based flood mapping is not feasible, is not only a matter of scientific realism, but ultimately increases the trust of users in the flood delineation products. In this context, one of the "output layers" provided by the Copernicus Emergency Management Service's recently released Global Flood Monitoring (GFM) product, is an "Exclusion Mask" which excludes such areas that are challenging for SAR (https://emergency.copernicus.eu/).

GFM is an online system that provides, as its main output, worldwide flood delineations by automatically ingesting and processing in near-real-time, all incoming Sentinel-1 SAR acquisitions. As part of the GFM methodology, as soon as a new Sentinel-1 image is available, the raw SAR backscatter data is promptly processed by three separate state-of-the-art flood

classification algorithms, in an unsupervised manner. The final flood map is generated via an ensemble approach that increases the robustness and reliability of the final products (Salamon et al., 2021; Krullikowski et al., 2023), together with a series of additional output layers (including the Exclusion Mask).

Water depth is considered to be the most informative proxy variable for quantifying flood impacts. In fact, empirical depth-damage curves have traditionally been designed to quantify economical losses as a function of water depth, for different exposed assets in different regions (Jongman et al., 2012; Huizinga et al., 2017). Despite the best practices and most recent advances, water depth cannot be estimated by satellite-based flood mapping.

Water depth estimation and the accurate identification of flood extent are critical tasks, not only for disaster risk manage-ment, but also for other scientific disciplines, including geomorphology, hydrology and climate change analysis (e.g. Feyen et al. (2020); Rossi et al. (2023)). Traditional approaches for estimating water depth and flooded area rely on ground-based observations and manual measurements, which suffer from limitations such as time-consuming data collection and limited spatial coverage. Remote sensing technologies and digital terrain models (DTMs) have recently opened promising avenues for addressing these challenges (Fuentes et al., 2019; Khattab et al., 2017).

For example, Cohen et al. (2018) developed an effective framework to compute flood depths using elevation derived from the intersection of flood delineation polygons and a DTM. A second release of the methodology (Cohen et al., 2019) improved some of the limitations of the first release, such as the computational inefficiency and the impossibility to properly consider the boundaries between floods and permanent water bodies. However, the framework still suffers from substantial processing times over very large areas (or with high resolution rasters) and can provide unrealistic water levels and depths in certain conditions. Other approaches for estimating flood depths at a local scale have proved effective (Bryant et al., 2022; Cian et al., 2018). Nevertheless, their applicability for large-scale assessments has not yet been proven. Furthermore, these approaches are rather elaborate, and are unlikely to be suitable for unsupervised use over large areas. Finally, none of the current methodologies takes advantage of topographical information to enhance flood delineations in a non-trivial manner (i.e. other than with so-called "bathtub model" approaches), nor have they been tested in complex riverine environments with irregular topographies, or they employ closed-source/commercial softwares (Rodriguez Enriquez et al., 2023).

To bridge the above-mentioned limitations, the current study introduces a new algorithm, named FLEXTH, the special feature of which is the exploitation of topographic information for working with flood maps containing gaps, due to excluded areas and/or seasonal or permanent water bodies. The goal is to expand the flood delineation and to provide estimates of water level and water depth seamlessly across the entire flood extent. The combined use of satellite-derived inundation maps and DTMs not only improves the overall accuracy and reliability of the flood assessment, but also enhances the ability to model and predict flood dynamics in areas prone to inundation. Furthermore, the framework is suitable for any flooding mechanism, namely riverine, costal and pluvial. Other key features of the methods described in this paper are: i) a limited requirement for supervision since the framework is designed to operate automatically over large areas; ii) computational efficiency, which is achieved using computer vision algorithms that entail reasonable processing times, for areas of up to tens of thousands of square kilometers.
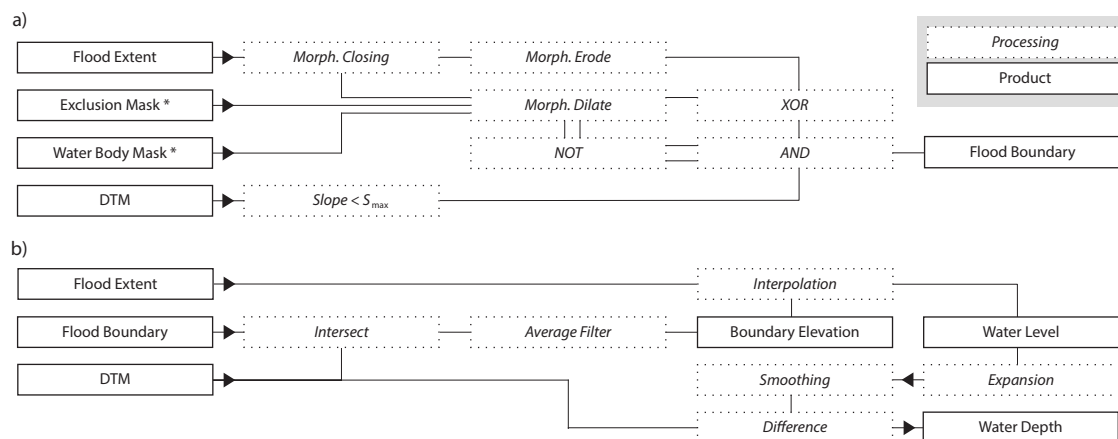
Figure 1. Workflow conceptualizing the main processing steps and the final/intermediate products: a) identification of valid wet-dry boundaries of flooded areas; b) computation of the water level and water depth in the initial and expanded flooded areas. Asterisks denote optional information, see Section 2.1.

90   The overall workflow that is presented in this study provides a comprehensive and efficient approach for enhancing (satellite-based) flood maps, and for complementing flood extent information with estimates of water level and water depth, with potential improvements to flood assessment, impact calculation and disaster response strategies.

2   Methods

The required and optional input data for the workflow illustrated in Figure 1 are introduced in Section 2.1. Section 2.2 describes
95   the procedure that estimates water level and water depth in areas initially delineated as flooded. Finally, in Section 2.3 the routine that propagates the flood water inside the exclusion mask by taking advantage of a DTM is described. Note that this final aspect is only relevant if an exclusion mask is provided as input.

The underlying algorithm (named FLEXTH) is available as an open access Python script (see the code availability section). An additional script is provided for easily preprocessing the input data (i.e. cropping, resampling and reprojecting the DTM to
100   the same grid as that of the flood delineation raster).

2.1   Input and Output products

The processing chain has, as a minimum requirement, two inputs: i) a binary raster map delineating the flooded areas; ii) a DTM (Figure 1). Additionally, users can take advantage of two optional input data layers: iii) an exclusion mask, which is a binary map delineating all areas excluded from flood mapping); iv) a binary map identifying permanent and seasonal water
105   bodies. The exclusion mask is particularly relevant when a satellite-borne sensor is unable to discriminate reliably flooded areas due to, for example, low sensitivity or water-look-alike conditions. An exclusion mask may correspond to clouds in the case of

optical image data (e.g. from Sentinel-2), or to densely vegetated/urbanized areas in the case of SAR sensors (e.g. Sentinel-1). To highlight the full capabilities of the procedure, the reminder of the study will assume all four input layers to be available. Section 4 provides insights on how the use of just the two primary inputs (flood delineation and DTM) may affect the final

110   results.

All processing steps are computed on georeferenced arrays (geotiff) with matching pixels: i.e. the inputs share the same spatial extent, pixel size and projected reference system.

2.2   Water level and water depth estimation

Water level (WL) refers to the elevation of the water surface above an arbitrary vertical datum, while water depth (WD) is the

115   difference between the elevation of the water surface and the underlying terrain. The idea behind the water level estimation method presented here, is that within each contiguous (or connected) flooded area, water level is directly dependent on the ground elevation along the corresponding wet-dry boundary. In particular, along the borders of flooded areas, the water level must fall in the interval between the elevation of the last flooded pixel and the first non-flooded neighbouring pixel. The terrain contours of the flooded areas, including flooded (i.e. wet) and non-flooded (i.e. dry) pixels, is therefore critical. The following

120   steps describe how to link the wet-dry boundaries (obtained from flood inundation maps) with topographical information (from the DTM) in order to estimate the water levels for each contiguous flooded area.

The workflow, as illustrated in further detail in Figure 2, consists of two main phases. The first phase, shown in Figure 2c, focuses on identifying the reference outline of contiguous flooded areas. The second phase, shown in Figure 2d, uses the reference outline in combination with a DTM (see Figure 2b) to compute water level and water depth inside each flooded area.

125   On a computational level, the procedure takes advantage of the Open Source Computer Vision Library ((https://opencv.org/) which was developed to facilitate efficient image processing operations over large raster datasets (Bradski, 2000).

As a pre-processing step, two rounds of "morphological" closing (Gonzalez and Woods, 2018; Haralick and Shapiro, 1992) using a 3x3 cross kernel are performed on the initial flood delineation (Figure 1a). This procedure can be relevant especially for automatically derived flood maps, where flooded areas may feature small inaccuracies and noisy borders. In fact, the algorithm

130   regularizes the wet-dry contour and fills small gaps that could otherwise affect the following steps and reduce the quality of the final water depth estimates.

Afterward, the borders of flooded areas, including neighbouring wet and dry pixels, are identified by subtracting (logical XOR) a morphological erosion of the flood map from its morphological dilation. Both operations are performed using a 3x3 box kernel (see Figure 2b, steps i to iv).

135   However, flooded areas may not simply be enclosed by "valid" wet-dry boundaries, but they can also share borders with areas excluded from flood mapping (Exclusion Mask) or with permanent water bodies. In the first case, the true location of the wet-dry divide is unknown, as it may be hidden inside the "blind" excluded areas. In the second case, when a flood merges with a water body, the shared wet-wet boundary doesn't provide any topographic information useful for determining the water level. For the identification of reliable water levels, it is therefore crucial to consider just the informative borders, and to exclude the

140   spurious ones. For this purpose, a dilation of both excluded areas and water bodies (with a 3x3 kernel) is used to mask the

wet-dry contours identified previously (Figure 2c, steps iv to vi). This operation correspond to combining with a logical AND the initial outline of flooded areas with the complement (i.e. logical NOT) of the dilated exclusion and water bodies mask, as per Figure 1a.

Additionally, border pixels corresponding to topographic gradients larger than the user-defined threshold S_{max} are excluded from the following computations (Figure 1a). In fact, large topographic gradients along the wet-dry boundaries, especially in combination with coarse resolutions of the input flood map and/or DTM, can lead to erroneous estimates of representative water levels (Cohen et al., 2022).

Because water level ideally lie between the elevations of neighboring wet-dry pixels, the DTM values corresponding to the remaining valid contour pixels are processed with a moving average filter (3x3 box kernel) in order to compute the representative water level along the outlines of the flooded areas (red dashed boxes in panel viii) of Figure 2d, see also Figure 2b).

The representative water level corresponding to the flooded/non-flooded boundaries are now used to extrapolate the water level inside each flooded area (step ix in Figure 2d). Each contiguous flooded area is first identified by means of a connected component analysis and processed independently (Stockman and Shapiro, 2001). For processing the pixels, a 4-connectivity rather than 8-connectivity approach is used to maximize the number of independent flooded areas.

The water level of each flooded pixel can then be estimated based on two alternative methodologies. Method A estimates water level at a target pixel as the distance-weighted arithmetic mean of the N closest pixels (in the Euclidean sense) belonging to the border of the corresponding flooded area. The weight $w = 1/d^{\alpha}$ is controlled by the parameter α which modulates the range of influence of each pixel of the border having a distance d from the target location. Alternatively, Method B requires the selection of an arbitrary percentile P of the distance-weighted distribution of the elevations along the border pixels as a reference for assigning water levels. Inverse-distance weighted percentiles are computed by scaling the frequency of the elevation of each pixel along the border by a factor $1/d^{\alpha}$. In general, Method A tends to provide smoother estimates of water levels. However, Method B can be more robust and versatile when the altimetry of the cells along the border is biased or is poorly representative of the actual water level. This may be due, for example, to inaccuracies in the delineation of flooded areas and/or errors in the DTM, or in case of coarse raster resolutions (Cohen et al., 2022).

If the number of pixels along the wet-dry boundary is too small to provide robust estimates of the water level inside a contiguous flooded area (say they are less than N_{min}), an alternative approach is adopted. Specifically, in these cases the water level is set as the P^* percentile of the distribution of DTM values inside that flooded region. Such an alternative approach is more likely to be required in the presence of small flooded areas located in steep topographies surrounded by extensive water bodies and/or excluded areas.

Finally, where the estimated water level is lower than the ground elevation, a fictive water depth WD^* is assigned. For consistency, the same WD^* is also added to the remaining water depth estimates. Water level estimates lower than ground elevation can occur (albeit rarely) in practice, for example, as a result of: i) imprecise flood delineation; ii) inaccuracies in the DTM; iii) vertical curvatures of the water surface due to hydrodynamic effects.
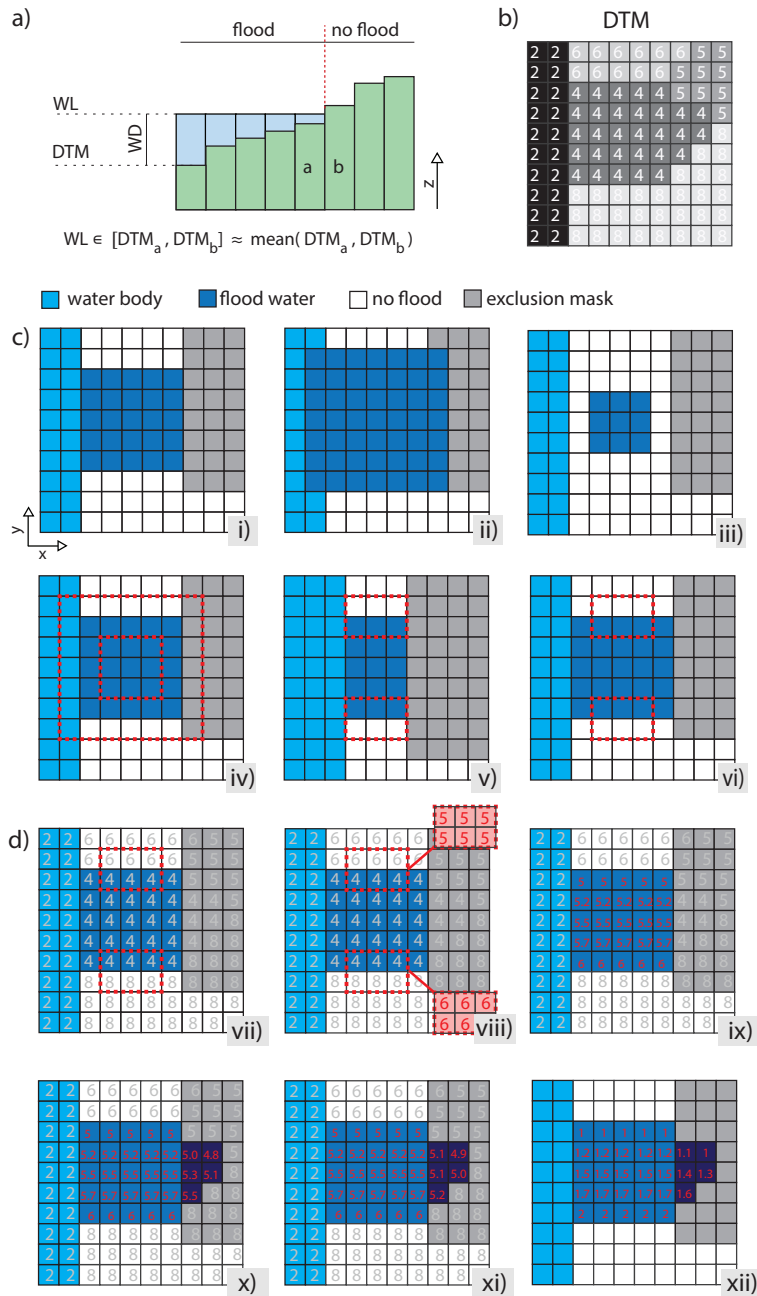
Figure 2. Schematic representation of the main steps of the procedure to estimate water depths and to expand floods inside excluded areas: a) principle behind the water depth estimation combining a flood map and a DTM; b) sample DTM with elevation values in each cell; c) identification of valid wet-dry boundaries of a flooded area; d) water level and water depth estimation and flood propagation in the exclusion mask.

2.3 Flood expansion

Once water levels are computed in each initially-delineated flooded areas, water is recursively spread from flooded pixels into neighboring masked (i.e. excluded) pixels, provided that the ground elevation of the excluded pixel is lower than the water level in the nearby source pixel (see Figure 2d, steps x-xi). To prevent unlimited and unrealistic spreading of flood water, a routine regulates water levels and allows water to spread up to a maximum distance (computed from the point along the initial flood boundary where flood propagation originated). In fact, without a constraint on flood spreading – such as in the case of a horizontal water level propagation as in a bathtub filling approach – flood water could propagate indefinitely. Such a risk may especially arise when extensive excluded areas are combined with regional topographical gradients or in large-scale assessments.

A maximum propagation distance d_{max} is assigned to each contiguous flooded area as a function of its extension A (km^2), allowing large flooded areas potentially to spread further. Specifically, flood expansion is controlled via the exponential relationship:

$$d_{max}(A) = D_{max}\left(1 - 2^{-\frac{A}{A_{1/2}}}\right) \tag{1}$$

where D_{max} (km) corresponds to the maximum allowable propagation distance for an arbitrarily large flooded area, and $A_{1/2}$ (km^2) establishes the flood extent for which $d_{max} = D_{max}/2$. This simple parameterization is heuristically rooted in the mass conservation principle: large flooded areas contain more water that can potentially propagate further. However, a sill is enforced as – in reality – flood propagation cannot increase indefinitely.

To improve computational efficiency and speed, flood propagation follows a basic forward explicit scheme which ensures a progressive decrease of water depth as the flood spreads. The numerical method begins by propagating water levels to neighbouring excluded pixels starting from the contours of each flooded area, and it continues until a set of conditions is met. In particular, starting from a generic pixel at position i, j, the algorithm estimates water levels in neighbouring excluded pixels at position $i \pm 1, j \pm 1$ ($WL_{i \pm 1, j \pm 1}$) based on the ground elevation $DTM_{i \pm 1, j \pm 1}$, the initial water level WL_0 at the origin of the propagation, and the distance $d_{i \pm 1, j \pm 1}$ computed along the propagation route until position $i \pm 1, j \pm 1$. Valid pixels where flood propagation is performed are those fulfilling all the following conditions: i) belong to the exclusion mask; ii) $DTM_{i \pm 1, j \pm 1} < WL_{i,j}$; iii) $WL_{i \pm 1, j \pm 1} < WL_{i,j}$; iv) no flood propagation has yet been performed on the target location. All the eight pixels surrounding each starting location are considered as neighbours in order to maximize spreading (8-connectivity). Specifically, the routine follows the expression:

$$WL_{i \pm 1, j \pm 1} = WL_0 - (WL_0 - DTM_{i,j})\frac{d_{i \pm 1, j \pm 1}}{d_{max}} \tag{2}$$

Figure 3 illustrates the behaviour of the flood propagation routine in a few one-dimensional sample cases. Specifically, the Figure shows how an initial water depth WD_0 propagates on different land surface topographies characterized by a starting value DTM_0 and a combination of a linear, a sinusoidal and a random trend parametrized via s_i, s_s and s_r as:
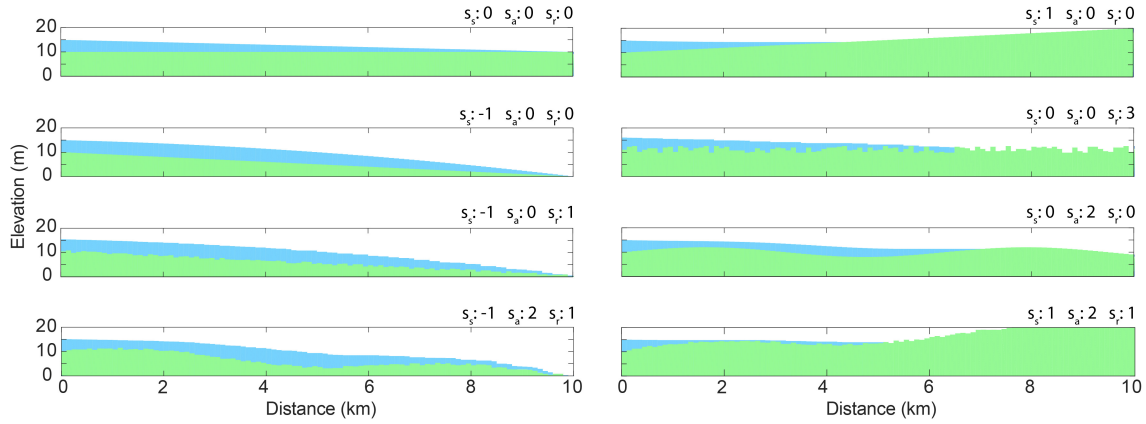
Figure 3. One-dimensional examples of the flood expansion routine over land surfaces featuring different topographies. Topographies are parameterized combining a linear trend s_i (‰), a sinusoidal component with amplitude s_s (m) and period 2π, and a random component ($z_{rand} \sim s_r \, \mathcal{U}(-0.5, 0.5)$ with s_r (m) as scale). Flood water propagates from left to right, starting from $WD_0 = 5\,m$ and $DTM_0 = 10\,m$ until the maximum assigned propagation distance $d_{max} = 10\,km$. Note that d_{max} can be reached just under some topographical conditions.

$$DTM(x) = DTM_0 + \frac{s_i}{1000}x + s_s \sin\left(\frac{2\pi x}{1000}\right) + s_r z_{rand} \qquad (3)$$

where x is a longitudinal dimension (in meters) and z_{rand} is a uniformly distributed random number in the interval $[-0.5, 0.5]$ (see caption of Figure 3 for details).

As a final post-processing step, water level estimates in the expanded regions are smoothed in order to: i) reduce poten-
210 tial discontinuities between the elevation of the water surface and the ground elevation in contiguous non-flooded pixels; ii) homogenize water levels where floodwaters spreading from different sources merge together. For this purpose, a 5x5 circular convolutional smoothing filter is slid twenty times over WL', i.e. the union between the estimated water level map and the DTM in non-flooded areas. Specifically, $WL' = WL(flood = 1) \cup DTM(flood = 0)$, where WL can in turn be seen as the union between water levels estimated inside the initially flooded areas (WL_0) and the water levels in the expanded flooded
215 areas (WL_e). At each recursive application of the filter, the initial values of $DTM(flood = 0)$ and WL_0 are reestablished, ensuring this post-processing step to be limited to WL_e. The procedure terminates with the last step of Figure 2d, where water depth is estimated as the difference between water level and the DTM.

3   Results: the Pakistan 2022 case study

The framework described in Section 2 is tested for the use case of the devastating floods that hit the Indus valley in Pakistan
220 between July and September 2022. The flood caused severe destruction, affected about 33 million peoples, claiming over 1700 victims, causing about 20 billion euros of direct damages (Nanditha et al., 2022). Given the severity and the wide extent of the

Table 1. Parametrization of the workflow used in the case study. Water depths and water levels are estimated using Method A (see Section 2).

Parameter	Description	Value	Units
S_{max}	Maximum admissible slope for the wet-dry reference border pixels	0.1	-
N_{max}	Maximum number of border pixels used to estimate WLs	100	-
N_{min}	Minimum number of valid border pixels required to estimate WL based on the default procedure	10	-
P^*	Percentile of the distribution of ground elevation underneath a flooded area used as a reference to estimate WL (alternative procedure)	0.98	-
α	Inverse distance weighting rate for WL interpolation within flooded areas	2	-
WD^*	Additional water depth assigned to account for WL estimates lower than ground elevation	0.1	m
D_{max}	Maximum propagation distance for an arbitrarily large flooded area	10	km
$A_{1/2}$	Initial size of a flooded area for which $d_{max} = D_{max}/2$	100	km^2

event – which was by far the world's largest flood during the period of the current study – it is well suited as a proof of concept for the methodology introduced in this study.

225   Specifically, the procedure described in the previous section is coupled with the maximum flood extent derived by aggregating over the months of July, August and September all flood delineations provided by GFM. The exclusion mask and water bodies are also based on GFM, whereas topographic information are provided by FABDEM, a recently released DTM whose goal is to remove vegetation and buildings from the Copernicus DEM by using AI and ancillary satellite data (ESA, 2022; Hawker et al., 2022).

    Figure 4 displays the flooded area and the corresponding water depth computed as described in Section 2 over the most
230   severely affected region. The result – featuring the morphology-based flood expansion – covers a total flooded area of 61331 km^2 (including neighboring flooded areas not shown in the Figure), which is about 50 % larger than the initial GFM-based flood delineation (39333 km^2). The results correspond to the parametrization summarized in Table 1. The sensitivity of the proposed methodology on model parameters is discussed in Section 4.

    The full running time featuring flood expansion and water depth estimation required to generate the result displayed in
235   Figure 4 is about 1.5 hours on a 6 Core CPU workstation (Intel Xeon C5-2620 v2) with 44 Gb of RAM.

3.1   Evaluation of the estimates of flood extent and water depths

In this section, the performance of the framework presented in Section 2 is evaluated quantitatively. In particular, subsection 3.1.1 and 3.1.2 focus on evaluating the flood extent, and the estimates of flood depth respectively. It is worth noting that ground truth derived via observations acquired during field surveys are rarely available for flood extents, and are even more scarce for
240   water level and depth– especially at the scales considered in this study. Furthermore, despite the long timescale of the event, reference data might display flood conditions at different stages.
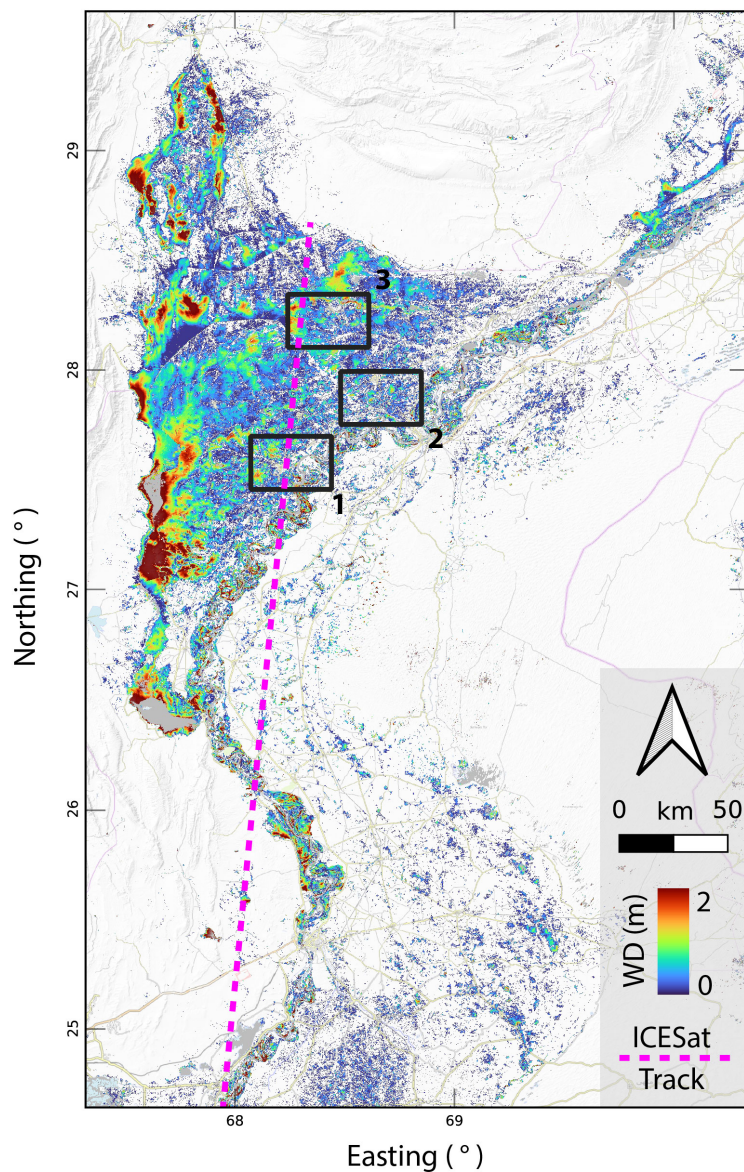
Figure 4. Flood delineation featuring flood expansion and water depth calculation as described in Section 2 over the most affected area along the Indus valley (Pakistan) during the flood of July-September 2022. Permanent and seasonal water bodies are depicted in gray. The three areas of interest (AOIs) are also highlight.

3.1.1 Evaluation of flood extent

The accuracy of flood extent delineation is evaluated using, as a reference, the flood maps produced by CEMS corresponding to the three AOIs delineated in Figure 4 (EMSR629 activation, https://emergency.copernicus.eu/mapping/list-of-components/

Table 2. Classification accuracy metrics of the flood maps displayed in Figure 5: Critical Success Index (CSI); User Accuracy (UA) and Producer Accuracy (PA) with respect to the " flood" class; relative frequency of True Positive (TP), True Negatives (TN), False Positives (FP) and False Negatives (FN). In parentheses are the metrics for the GFM flood delineation without flood expansion (i.e. first column in Figure 5).

	CSI (%)	UA (%)	PA (%)	TP (%)	TN (%)	FP (%)	FN (%)
AOI 1	69 (65)	77 (81)	88 (77)	51 (44)	26 (31)	16 (11)	7 (13)
AOI 2	68 (58)	85 (88)	76 (63)	54 (43)	21 (24)	9 (6)	15 (26)
AOI 3	63 (63)	65 (68)	94 (89)	52 (48)	18 (23)	28 (22)	3 (6)

245 EMSR629). The maps cover 3000 km^2 in total, and aim to capture the maximum flood extent around the cities of Larkana (AOI 1), Shikarpur (AOI 2) and Jacobabad (AOI 3). The CEMS maps in vector format (i.e. shapeflies) were produced in a semi-automatic/semi-supervised way with expert knowledge refinement starting from the imagery acquired by the SPOT6/7 sensor on the 30th of August 2022 (Roth et al., 2022).

 Figure 5 compares the CEMS flood delineation against the flood classification obtained by the temporal merging of the GFM
250 flood extent layers (first row), as well as the GFM-based flood expansion procedure described in Section 2 (second row). For completeness, the third and the fourth rows of Figure 5 displays the water level and the water depth estimates obtained with the entire workflow described in the methods sections (including flood expansion). Table 2 summarizes the performances of the classification for the two different scenarios (i.e. with and without flood expansion) for all three AOIs.

3.1.2 Evaluation of water depth estimates with ICESat-2

255 This section describes the approach developed to assess the water depth estimates computed in Section 2, using as a benchmark the altimetric data acquired by the ICESat-2 satellite mission of NASA (https://icesat-2.gsfc.nasa.gov). Specifically, ICESat-2 features ATLAS, an accurate laser altimeter designed for worldwide recording along six parallel tracks of ground points at a sampling frequency of up to about 1 point/m and a revisit time of 91 days (Neuenschwander and Pitts, 2019; Dandabathula et al., 2023; Wang et al., 2019; Li et al., 2021).

260 ICESat-2/ATLAS delivers twenty-two standard products (i.e. ATL00 - ATL21) divided into four levels (i.e. levels 0 - 3) characterized by increasing levels of processing. The current analyses employ ATL03, a Level 2 product that maintains the full altimetric information after basic post-processing steps on the initial raw telemetry data (Zhu et al., 2022). ICESat-2 acquires altimetric data along three pairs of tracks, each pair being characterized by a weak and strong beam of photons (4:1 energy ratio). Pairs of tracks are 3.3 km apart in the across-track direction, while strong and weak beams have a transversal offset of
265 90 m. For the analysis, only medium and high confidence photons from the strong beams are used.

 On the 3 September 2022, ICESat-2 acquired data along a 500 km track through the study area (see Figure 4). The timing of the acquisition is compatible with the maximum flood extent in the area, estimated to be around the end of August (Nanditha et al., 2022; Roth et al., 2022). Such data are used as a reference altimetry during the flood. Furthermore, two of the three strong tracks acquired by ICESat-2 on 3 September have a good spatial match (i.e. they are about 50 m apart in the across-track
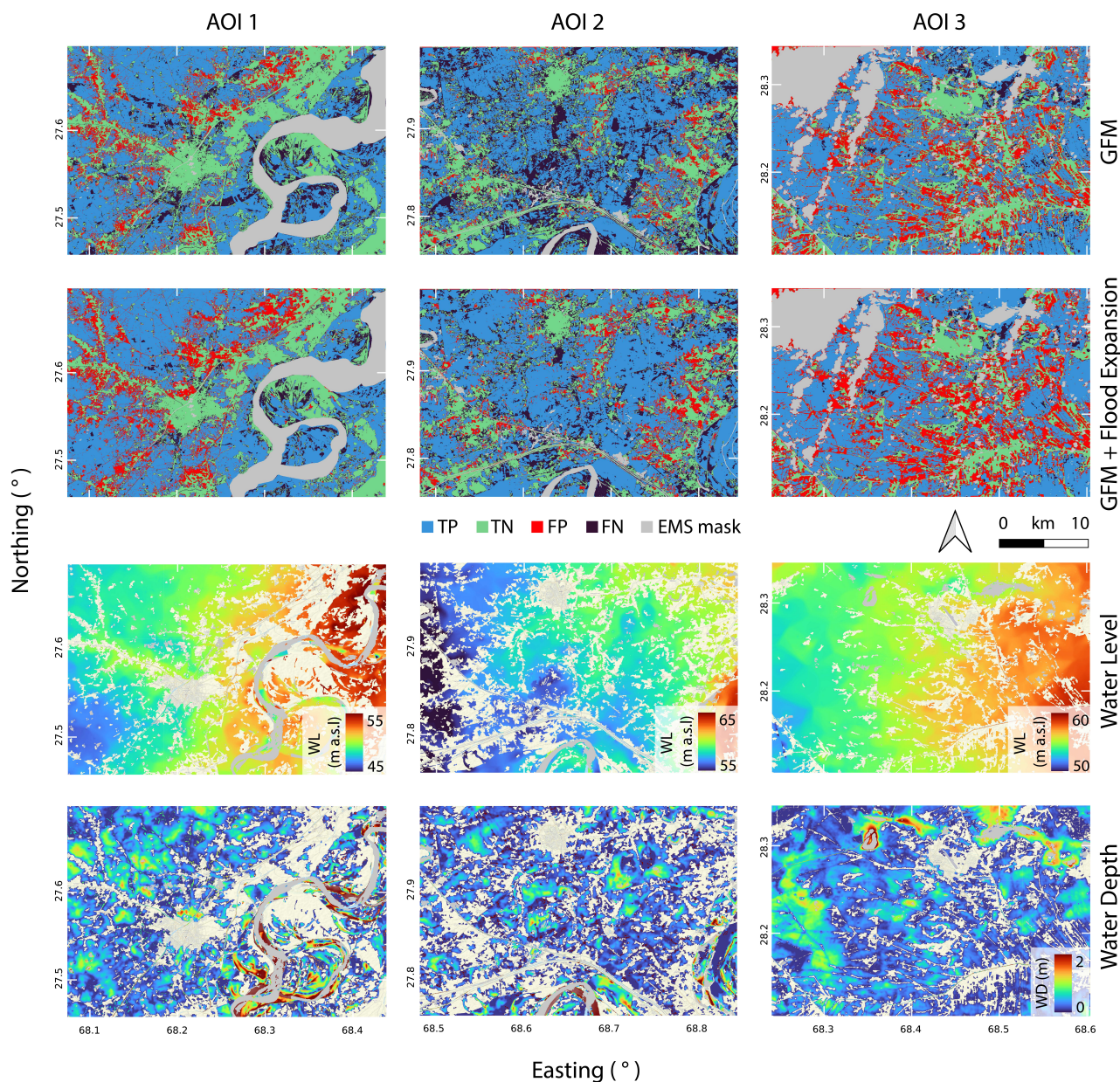
Figure 5. Classification results of: i) aggregated flood delineations obtained by merging GFM products over the months of July, August and September 2022 (first row), and ii) the flood expansion procedure described in Section 2, (second row) for the 3 AOIs considered. Classification performances are displayed in terms of true positives (TP), true negatives (TN), false positives (FP) and false negatives (FN) with respect to the reference CEMS rapid mapping products (activation: EMSR629). Panels in the third and fourth rows: water level and water depth computed following the procedure outlined in Section 2. See Table 2 for an explanation of the classification accuracy metrics.

270   direction) with two of the strong tracks acquired by ICESat-2 on the 6 June 2021. Each pair of spatially matching ICESat-2 tracks during the flood period (September) and during the dry period (June) are denoted as I_{wet}^i and I_{dry}^i respectively, with $i = 1, 2$. The wet (dry) tracks feature a total of about 1 (0.8) million points, with an average spacing of 0.31 (0.62) m and similar inter-quartile ranges of about 0.71 m for both tracks.

As described below, the altimetric data acquired by ICESat-2 during the dry and wet conditions are used to assess water

275   depth estimates computed as described in Section 2. In particular, I_{dry}^i serves as a reference ground topography, whereas I_{wet}^i is expected to be positively biased by flood water.

As a preparatory step for the analyses, the I_{dry}^i and I_{wet}^i tracks are processed with a moving median filter (with a window over 100 photons) in order to minimize the noise which characterizes the data and to reduce potential biases caused by vegetation and/or buildings. The filtered photons – which are irregularly spaced along the tracks – are then resampled on the same $5 \cdot 10^{-5}$

280   degrees latitude intervals (about 5 m). As ICESat-2 follows a north-south orbit, altimetric observation at resampled locations correspond to the same latitudes, while longitudinal differences are due to the ~50m offset between I_{dry}^i and I_{wet}^i. As a result, resampled altimetric information from the dry and wet tracks represent surface elevation at approximately the same locations.

Considering the water depths (WDs) computed as described in Section 2 and sampled in correspondence of the I_{wet}^i photons, Figure 6a and b display the distribution of the difference $\Delta = I_{wet}^i - I_{dry}^i$ and $\Delta = I_{wet}^i - \left(I_{dry}^i + WD \right)$ for all flooded pixels

285   delineated in Figure 4. The distribution of the elevation differences highlights the fact that including water depth estimates based on the proposed procedure substantially reduces both the bias and the variability in the distribution of Δ. Furthermore, the mode of the distribution correctly matches 0 when water depth estimates are added to the ground elevation measured by ICESat-2 during dry conditions.

To conclude, the distributions in panels c d and e of Figure 6 compare ICESat-2 altimetry both in absence of flooding (I_{dry})

290   and in flood condition (I_{wet}) with FABDEM. Panel c shows that along the sampled points FABDEM has a small positive bias compared to ICESat-2 and a fairly symmetrical distribution during dry conditions. On the other hand, as expected, during the flood the distribution shifts towards larger values of I_{wet} with a substantial skewness in the distribution. Adding the water depth estimates effectively reduces the bias (panel e), but underestimated flood depths remain.

4   Discussion

295   Despite the complex flooding pattern, the water depth and water level estimates, together with the enhanced flood extent displayed in Figure 4 and 5, appear to be realistic, highlighting the potential of the procedure outlined in this study. The quantitative evaluation of the results confirms this first impression. Figure 5 shows that the Sentinel-1 derived flood delineation, automatically delivered by GFM already matches well the CEMS maps for all three AOIs (Table 2). Further enhancing the flood delineation, following the procedure described in this study, enlarges flooded areas and reduces false negatives. Despite the

300   increased number of false positives due to the flood expansion, it should be noted that CEMS flood maps (used as "ground truth" reference) are likely to suffer from underestimations, as they are derived based on the Airbus SPOT 6/7 optical sensor. In fact, similar to radar sensors, optical sensors may be inadequate to detect flood water under vegetation and in urban areas.
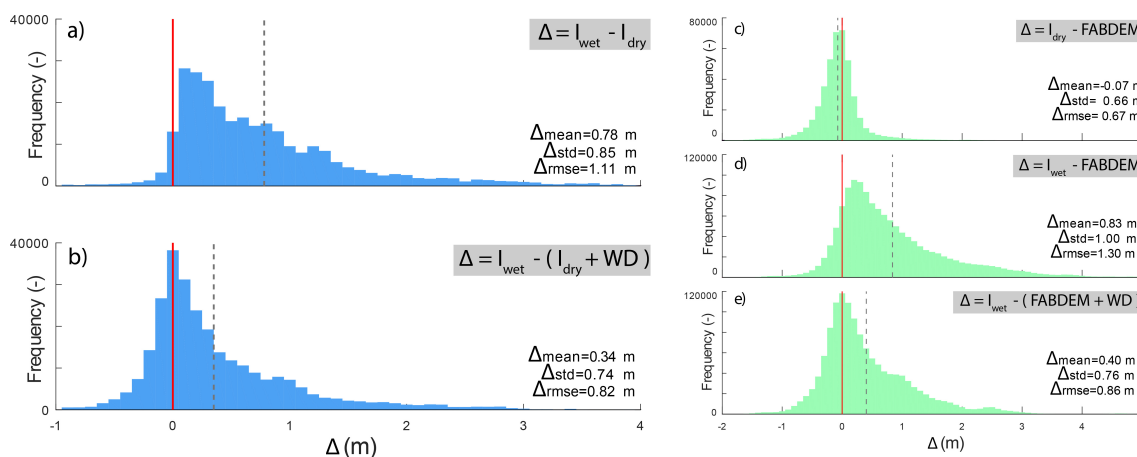
Figure 6. Distribution of the difference between altimetric data acquired by ICESat-2 during wet and dry conditions along a 500 km track across the study area with (or without) considering water depth estimates (panels a and b). Comparison of the ICESat-2 altimetric data with FABDEM in wet and dry conditions including (or not) water depth estimates (panels c d and f). The red vertical bar highlights the ideal condition, while the dashed line corresponds to the mean of the distribution.

Despite the efforts to identify and exclude areas where flood mapping cannot be performed reliably, CEMS products still have difficulty identifying all such areas, and some areas that are not excluded may actually be flooded. In contrast, the flood
305 expansion procedure, because it has a physically-based component relying on ground topography, may be better suited for capturing floods in non-sensitivity areas.

Evaluating water depth estimates in flood maps is a challenging task: no direct or indirect measures of water level and/or water depth are generally recorded, especially over such large areas and in underdeveloped regions. Nonetheless, the methodology proposed here to estimate and assess water depth highlights the added value of the framework, and the consistency of
310 water depth estimates with ICESat-2 measurements. The 91-days revisit time of ICESat-2 reduces the chances of a temporal match between a flood peak and an altimetric acquisition. Furthermore, for the mid-latitudes (approximately 60S to 60N) laser beams operate off-nadir in order to increase spatial sampling. Considering the narrow diameter of laser pulses (about 17m), this implies that repeated cycles of the very same locations are practically impossible. Nonetheless, the current procedure, which considers two closely located acquisitions during the flood and non-flood periods, is reasonable for benchmarking purposes (at
315 least on floodplains) because of the reduced topographic gradients.

The limitations of the current approach are related to the accuracy and resolution both of the input flood delineation and of the underlying DTM. Although flood depth at each pixel is estimated using the elevation of multiple locations along the contours of flooded areas in order to improve robustness, inaccuracies in the identification of the correct wet-dry divide may lead to erroneous water depth estimates, particularly in steep terrains. Large errors in water depth estimates are less likely in flat
320 areas because of the reduced sensitivity of water level estimates to potentially erroneous flood delineations. However, where topographical gradients are reduced, even small differences in water depth estimation can lead to floods propagating over very

different extents. The DTM accuracy and resolution are also critical, as they are key in water level, and in turn, in water depth estimation. In fact, even assuming a perfect delineation of flood waters, a coarse DTM in steep areas can strongly affect the resulting water levels.

325   It is also worth noting that maximum flood extents obtained via spatio-temporal merging of multiple flood delineation products can be inaccurate, as it can contain singular features (e.g. sharp edges). This aspect is relevant when the spatial scale of the flood is much larger than the imagery footprint used for flood delineation, and in the case of large temporal gaps between neighbouring acquisitions.

The underestimated water depths shown in Figure 6 b and e are likely to be related to underestimated flood extents and/or

330   the fact that the ICESat-2 acquisition was nearer to the flood peak, compared with the Sentinel-1 imageries used by GFM to compute the initial flood extent. In fact, even using a larger percentile (say 0.75) of the distribution of ground elevation along the contour between flooded and non-flooded areas to estimate water levels, as per Method B (see Section 2.2), alleviates but does not solve the problem. This suggests that the underestimation is associated with the available input data, rather than a systematic negative bias of the methodology.

335   The flood expansion routine described in this study requires, as optional inputs, an exclusion and a water body mask. While water depth estimation can still be performed in the absence of such inputs, it is worth noting that water level and water depth may be underestimated in areas featuring extensive interfaces between flood water and permanent waters, and/or where accurate flood mapping is impeded by dense vegetation or buildings. If the borders between flood water and no-sensitivity areas are not excluded, they will contribute to the estimation of water levels. In these settings, ground elevations used as a reference

340   to compute water level will not correspond to the real wet-dry border (which in reality would be outside the flooded area and at higher elevation), therefore leading to underestimated water levels. Thus, especially in case of costal flooding, it is paramount that the water mask corresponding to the sea is covering (or properly matching) the seaward outline of the flood delineation.

The methods described in this study include several user-defined parameters. Such parameters can enhance the power and the flexibility of the framework. The heuristically selected set of parameters in Table 1 led to adequate performances across

345   multiple case studies and, overall, results are consistent across a wide range of parameter values. However, parameter selection may suffer from a degree of arbitrariness. For the water level and water depth estimation routine, the most critical parameters are found to be: S_{max}, N_{max}, α and P. The threshold for terrain slope, S_{max} used to exclude steep pixels from being used as a reference for water level estimation, has to be a trade-off between too conservative (low) and too permissive (large). Low S_{max} will reduce the number of pixels available for water level estimation, ultimately losing valuable altimetric information.

350   On the other hand, a high S_{max} may allow non-representative pixels to contribute for water level estimation. The selection of S_{max} has also to account for the pixel size, as even a small threshold associated with a coarse DTM can lead to large vertical inaccuracies. The maximum number of pixels used to estimate water level at a target flooded location (N_{max}) is also relevant. Our tests showed that results are consistent, for N_{max} in a range between 50 and 200, but at the upper end of the interval the role of α also becomes critical. Appropriate results have been found for $\alpha \in [1,3]$. Lower values of α use more information

355   of the altimetry along a larger share of the flood borders and provide smoother water level estimates. However, they may also include distant borders that do not well represent water level at a given target location. On the contrary, by giving more weight

to the nearest border pixels, high α can capture better the smaller-scale variability of the water level (although water level estimates can be more prone to local errors in the DTM and/or flood delineation). Larger N_{max} and smaller α may be required to produce smoother and more realistic water level and water depth estimates when Method B is employed. The percentile P

360 of the distance-weighted distribution of reference pixels elevations used to estimate water level according to Method B (see Section 2.2), is also relevant. This parameter offers additional flexibility as it can be used to compensate for potential systematic biases of flood extent maps, or it can be employed to assess different scenarios. Water level estimates using Method B can be more robust when flooded areas are surrounded by steep terrains, as water level is computed based on the percentiles of the altimetric distribution of the wet-dry contour. However, using large percentiles (say above 75 %) may lead to erroneous and

365 exaggerated flood propagation, triggered by overestimated initial water levels under some topographical conditions. On the other hand, our tests showed limited sensitivity of the results on the shapes of the kernels as well as on the type of connectivity used for the spatial analyses (see Section 2.2 and 2.3).

The flood propagation routine itself should also be critically assessed. Despite following simple physically based principles, it extrapolates information where no flood mapping is available. Especially in presence of regional topographical gradients and

370 extensive excluded areas, floods can potentially propagate across large areas up to large distances. Improved flood mapping, DTMs, and limiting the extent of areas excluded from mapping, will strongly constrain flood propagation and limit potential misbehaviours. Furthermore, the two parameters controlling flood propagation (especially D_{max}) offer adequate flexibility to control flood propagation under different circumstances, and can be tweaked as desired.

Additional analyses are envisaged for the future to further explore the role of model parameters. However, it has to be stressed

375 that ideal parameter values may depend on local conditions, and also on the accuracy and resolution of both the available flood delineation map and of the underlying DTM. For this reason, a "one-fits-all" approach in selecting the optimal parameter might be unrealistic.

Finally, it is worth stressing that the approach can be applied to any flooding mechanisms, including floods in costal settings. Costal areas can present favourable conditions for the application of the methodology. In general, coasts do not display

380 topographical gradient which may challenge the flood propagation routine as the regional ground elevation tend to increase landward (constraining flood expansion). Furthermore, in costal areas, FLEXTH has to ingest a reduced variability of initial water levels as compared to riverine environments as surge run-up can range up to about 10 m (Fritz and Okal, 2008; Fritz et al., 2009, 2010; Liu et al., 2005). On the other hand, water levels along a flooding river can span hundreds of meters, depending on the regional slope and the scale of the event (e.g. over 100 m in the current case study).

385 **5   Conclusions**

The study presented a robust methodology – named FLEXTH – to estimate flood depth and to improve flood delineation based on satellite-derived inundation maps, readily available DTMs, and open source tools. The procedure requires minimum supervision and can run over extremely large areas in a reasonable amount of time.

The workflow starts by identifying suitable wet-dry boundaries from flood maps, which can be derived by any means (e.g. by satellites or aerial sensors, or ground surveys). By combining flood boundaries that are altimetrically informative with digital models of the land surface, the procedure extracts the ground elevation along the borders of connected flooded areas, regardless of the complexity of the flood outlines and the surrounding topography. At each flooded location, water levels are computed based on the distance-weighted reference elevations of multiple points along the wet-dry border. Water is then propagated in contiguous low-lying areas priorly excluded from flood mapping. Hydraulic connectivity is guaranteed by a recursive propagation algorithm, which additionally enforces a routine to realistically decrease water levels as propagation advances. Finally, flood water depths are obtained subtracting the underlying topography from the water surface elevation.

Flood extents and water depth estimates computed for the 2022 flood disaster that hit the Indus valley in Pakistan, were shown to match adequately the available benchmark data. These results are an encouraging starting point for a systematic application of the framework over large-sized data sources of flood extent maps, such as those from the recently released Global Flood Monitoring (GFM) of CEMS. Future development of the methodology will focus on systematically optimizing the parameters of the algorithm under different geographical conditions. Fine-tuning the architecture of the algorithm is also envisaged for future releases, possibly targeting the computational speed of the flood propagation component.

It is finally worth mentioning that FLEXTH can be effectively applied also to costal floodings, provided that a mask is assigned covering the sea surface.

Overall, the presented methods can assist emergency response planning, flood impact assessment, and contribute to reduce the disastrous consequences of floods worldwide, especially in the context of an increased flood risk caused by a changing climate.

Code availability. FLEXTH is available as a Python script on GitHub at https://github.com/AndBetter/FLEXTH. An additional script named "DTM_2_floodmap.py" is also provided to easily resample/reproject and align input data into the same grid and projected reference system as the flood delineating raster.

Author contributions. Conceptualization: AB; Data curation: AB; Formal analysis: AB; Investigation: AB; Methodology: AB; Project administration: PS; Resources: PS; Software: AB; Supervision: PS; Validation: AB; Visualization: AB; Writing - original draft preparation: AB; Writing: review and editing: AB, PS

Competing interests. The authors declare no conflict of interests.

Acknowledgements. ***

References

Bradski, G.: The OpenCV Library, Dr. Dobb's Journal of Software Tools, 2000.

Bryant, S., McGrath, H., and Boudreault, M.: Gridded flood depth estimates from satellite-derived inundations, Natural Hazards and Earth System Sciences, 22, 1437–1450, 2022.

Cian, F., Marconcini, M., Ceccato, P., and Giupponi, C.: Flood depth estimation by means of high-resolution SAR images and lidar data, Natural Hazards and Earth System Sciences, 18, 3063–3084, 2018.

Clement, M. A., Kilsby, C., and Moore, P.: Multi-temporal synthetic aperture radar flood mapping using change detection, Journal of Flood Risk Management, 11, 152–168, 2018.

Cohen, S., Brakenridge, G. R., Kettner, A., Bates, B., Nelson, J., McDonald, R., Huang, Y.-F., Munasinghe, D., and Zhang, J.: Estimating floodwater depths from flood inundation maps and topography, JAWRA Journal of the American Water Resources Association, 54, 847–858, 2018.

Cohen, S., Raney, A., Munasinghe, D., Loftis, J. D., Molthan, A., Bell, J., Rogers, L., Galantowicz, J., Brakenridge, G. R., Kettner, A. J., Huang, Y.-F., and Tsang, Y.-P.: The Floodwater Depth Estimation Tool (FwDET v2.0) for improved remote sensing analysis of coastal flooding, Natural Hazards and Earth System Sciences, 19, 2053–2065, https://doi.org/10.5194/nhess-19-2053-2019, 2019.

Cohen, S., Peter, B. G., Haag, A., Munasinghe, D., Moragoda, N., Narayanan, A., and May, S.: Sensitivity of Remote Sensing Floodwater Depth Calculation to Boundary Filtering and Digital Elevation Model Selections, Remote Sensing, 14, https://doi.org/10.3390/rs14215313, 2022.

Dandabathula, G., Hari, R., Ghosh, K., Bera, A. K., and Srivastav, S. K.: Accuracy assessment of digital bare-earth model using ICESat-2 photons: Analysis of the FABDEM, Modeling Earth Systems and Environment, 9, 2677–2694, 2023.

Douris, J. and Kim, G.: The Atlas of Mortality and Economic Losses from Weather, Climate and Water Extremes (1970-2019), 2021.

EMDAT: Disasters in numbers, Tech. rep., CRED, 2022.

ESA: Copernicus DEM, https://doi.org/10.5270/esa-c5d3d65, 2022.

Feyen, L., Ciscar Martinez, J. C., Gosling, S., Ibarreta Ruiz, D., Soria Ramirez, A., Dosio, A., Naumann, G., Russo, S., Formetta, G., Forzieri, G., Girardello, M., Spinoni, J., Mentaschi, L., Bisselink, B., Bernhard, J., Gelati, E., Adamovic, M., Guenther, S., de Roo, A., Cammalleri, C., Dottori, F., Bianchi, A., Alfieri, L., Vousdoukas, M., Mongelli, I., Hinkel, J., Ward, P., Gomes Da Costa, H., de Rigo, D., Liberta', G., Durrant, T., San-Miguel-Ayanz, J., Barredo Cano, J. I., Mauri, A., Caudullo, G., Ceccherini, G., Beck, P., Cescatti, A., Hristov, J., Toreti, A., Perez Dominguez, I., Dentener, F., Fellmann, T., Elleby, C., Ceglar, A., Fumagalli, D., Niemeyer, S., Cerrani, I., Panarello, L., Bratu, M., Després, J., Szewczyk, W., Matei, N., Mulholland, E., and Olariaga-Guardiola, M.: Climate change impacts and adaptation in Europe. JRC PESETA IV final report, JRC Research Reports JRC119178, Joint Research Centre (Seville site), https://EconPapers.repec.org/RePEc:ipt:iptwpa:jrc119178, 2020.

Fritz, H. M. and Okal, E. A.: Socotra Island, Yemen: field survey of the 2004 Indian Ocean tsunami, Natural Hazards, 46, 107–117, 2008.

Fritz, H. M., Blount, C. D., Thwin, S., Thu, M. K., and Chan, N.: Cyclone Nargis storm surge in Myanmar, Nature Geoscience, 2, 448–449, 2009.

Fritz, H. M., Blount, C., Albusaidi, F. B., and Al-Harthy, A. H. M.: Cyclone Gonu storm surge in the Gulf of Oman, Indian ocean tropical cyclones and climate change, pp. 255–263, 2010.

Fuentes, I., Padarian, J., van Ogtrop, F., and Vervoort, R. W.: Comparison of surface water volume estimation methodologies that couple surface reflectance data and digital terrain models, Water, 11, 780, 2019.

Gonzalez, R. C. and Woods, R. E.: Digital image processing, Pearson Education Ltd., 2018.

Grimaldi, S., Li, Y., Pauwels, V. R., and Walker, J. P.: Remote sensing-derived water extent and level to constrain hydraulic flood forecasting
455   models: Opportunities and challenges, Surveys in Geophysics, 37, 977–1034, 2016.

Haralick, R. M. and Shapiro, L. G.: Computer and Robot Vision, Addison-Wesley Longman Publishing Co., Inc., 1992.

Hawker, L., Uhe, P., Paulo, L., Sosa, J., Savage, J., Sampson, C., and Neal, J.: A 30 m global map of elevation with forests and buildings
removed, Environmental Research Letters, 17, 024 016, https://doi.org/10.1088/1748-9326/ac4d4f, 2022.

Huizinga, J., De Moel, H., and Szewczyk, W.: Global flood depth-damage functions: Methodology and the database with guidelines, Tech.
460   rep., Joint Research Centre (Seville site), 2017.

Jo, M., Osmanoglu, B., Zhang, B., and Wdowinski, S.: Flood extent mapping using dual-polarimetric Sentinel-1 synthetic aperture radar
imagery, 2018.

Jongman, B., Kreibich, H., Apel, H., Barredo, J. I., Bates, P. D., Feyen, L., Gericke, A., Neal, J., Aerts, J. C., and Ward, P. J.: Com-
parative flood damage model assessment: Towards a European approach, Natural Hazards and Earth System Science, 12, 3733–3752,
465   https://doi.org/10.5194/nhess-12-3733-2012, 2012.

Khattab, M. F., Abo, R. K., Al-Muqdadi, S. W., and Merkel, B. J.: Generate reservoir depths mapping by using digital elevation model: A
case study of Mosul dam lake, Northern Iraq, Advances in Remote Sensing, 6, 161–174, 2017.

Krullikowski, C., Chow, C., Wieland, M., Martinis, S., Bauer-Marschallinger, B., Roth, F., Matgen, P., Chini, M., Hostache, R., Li, Y., et al.:
Estimating ensemble likelihoods for the Sentinel-1 based Global Flood Monitoring product of the Copernicus Emergency Management
470   Service, arXiv preprint arXiv:2304.12488, 2023.

Li, B., Xie, H., Liu, S., Tong, X., Tang, H., and Wang, X.: A method of extracting high-accuracy elevation control points from ICESat-2
altimetry data, Photogrammetric Engineering & Remote Sensing, 87, 821–830, 2021.

Liu, P. L.-F., Lynett, P., Fernando, H., Jaffe, B. E., Fritz, H., Higman, B., Morton, R., Goff, J., and Synolakis, C.: Observations by the
international tsunami survey team in Sri Lanka, Science, 308, 1595–1595, 2005.

475 Nanditha, J. S., Kushwaha, A. P., Singh, R., Malik, I., Solanki, H., Chuphal, D. S., Dangar, S., Mahto, S. S., Vegad,
U., and Mishra, V.: The Pakistan Flood of August 2022: Causes and Implications, Earth's Future, 11, e2022EF003 230,
https://doi.org/https://doi.org/10.1029/2022EF003230, e2022EF003230 2022EF003230, 2022.

Neuenschwander, A. and Pitts, K.: The ATL08 land and vegetation product for the ICESat-2 Mission, Remote sensing of environment, 221,
247–259, 2019.

480 Pulvirenti, L., Pierdicca, N., Chini, M., and Guerriero, L.: An algorithm for operational flood mapping from Synthetic Aperture Radar (SAR)
data using fuzzy logic, Natural Hazards and Earth System Sciences, 11, 529–540, 2011.

Rodriguez Enriquez, A., Wahl, T., Talke, S. A., Orton, P., Booth, J. F., and Santamaria-Aguilar, S.: Matflood: An Efficient Algorithm for
Mapping Flood Extent and Depth, Available at SSRN 4375664, 2023.

Rossi, D., Zolezzi, G., Bertoldi, W., and Vitti, A.: Monitoring Braided River-Bed Dynamics at the Sub-Event Time Scale Using Time Series
485   of Sentinel-1 SAR Imagery, Remote Sensing, 15, 3622, 2023.

Roth, F., Bauer-Marschallinger, B., Tupas, M. E., Reimer, C., Salamon, P., and Wagner, W.: Sentinel-1 based analysis of the Pakistan Flood
in 2022, EGUsphere, 2022, 1–13, https://doi.org/10.5194/egusphere-2022-1061, 2022.

Salamon, P., Mctlormick, N., Reimer, C., Clarke, T., Bauer-Marschallinger, B., Wagner, W., Martinis, S., Chow, C., Böhnke, C., Matgen, P.,
et al.: The new, systematic global flood monitoring product of the copernicus emergency management service, in: 2021 IEEE International
490   Geoscience and Remote Sensing Symposium IGARSS, pp. 1053–1056, IEEE, 2021.

Schumann, G. J.-P. and Moller, D. K.: Microwave remote sensing of flood inundation, Physics and Chemistry of the Earth, Parts a/b/c, 83, 84–95, 2015.

Spasova, T. and Nedkov, R.: On the use of SAR and optical data in assessment of flooded areas, in: Seventh International Conference on Remote Sensing and Geoinformation of the Environment (RSCy2019), vol. 11174, pp. 268–278, SPIE, 2019.

495 Stockman, G. and Shapiro, L. G.: Computer vision, Prentice Hall PTR, 2001.

Voigt, S., Giulio-Tonolo, F., Lyons, J., Kučera, J., Jones, B., Schneiderhan, T., Platzeck, G., Kaku, K., Hazarika, M. K., Czaran, L., et al.: Global trends in satellite-based emergency mapping, Science, 353, 247–252, 2016.

Wang, C., Zhu, X., Nie, S., Xi, X., Li, D., Zheng, W., and Chen, S.: Ground elevation accuracy verification of ICESat-2 data: A case study in Alaska, USA, Optics express, 27, 38 168–38 179, 2019.

500 Zhu, J., Yang, P.-f., Li, Y., Xie, Y.-z., and Fu, H.-q.: Accuracy assessment of ICESat-2 ATL08 terrain estimates: A case study in Spain, Journal of Central South University, 29, 226–238, 2022.